RSC Advances

PAPER

View Article Online
View Journal | View Issue

Cite this: *RSC Adv.*, 2026, **16**, 12628

First-principles study of d^0 magnetism in a SnI_2 monolayer induced by P and As impurities

Pham Minh Tan,[a] Nguyen Thanh Son,[b] Duy Khanh Nguyen,[cd] J. Guerrero-Sanchez[e] and D. M. Hoat*[fg]

Received 5th December 2025
Accepted 9th February 2026

DOI: 10.1039/d5ra09400c

rsc.li/rsc-advances

Searching for d^0 magnetism in two-dimensional materials has attracted great attention because of its importance for next-generation spintronics. In this work, doping with pnictogen (X = P and As) atoms is proposed for engineering the magnetic properties of a SnI_2 monolayer. The pristine monolayer is a nonmagnetic semiconductor with a band gap of 2.03 eV. Magnetic states are induced by doping with a single pnictogen atom, where an overall magnetic moment of 2.00 μ_B is produced primarily by the impurity. In addition, the emergence of magnetic semiconducting behavior and in-plane magnetic anisotropy (IMA) is also confirmed. The study of spin coupling in pnictogen-doped SnI_2 systems demonstrates the effectiveness of X–X separation for controlling the electronic and magnetic properties. Specifically, an antiferromagnetic semiconducting nature is found to be stable with a small interatomic distance, while increasing the separation between the impurities induces a transition in the electronic behavior, resulting in ferromagnetic half-metallicity or ferromagnetic semiconducting character. In the latter case, large Curie temperatures of 282.20 and 462.66 K are obtained by P and As doping, respectively, indicating the robustness of the ferromagnetism. In addition, the X–X separation also significantly influences the magnetic anisotropy of the doped system. Specifically, perpendicular magnetic anisotropy (PMA) is obtained when two impurities are close to each other, whereas increasing the distance between them induces a PMA-to-IMA transition. Our findings provide insights into the electronic and magnetic properties of the SnI_2 monolayer upon doping with pnictogen atoms, suggesting that these efficient doping approaches can induce d^0 magnetism and enable promising applications in magnetic-field sensing and magnetoresistive random-access memory (MRAM) fabrication.

1. Introduction

Despite being investigated since the earliest decades of 20th century, two-dimensional (2D) materials have only been attracting continuously increasing interest since the successful isolation of graphene.[1] The graphene lattice is formed by carbon atoms situated in a planar honeycomb arrangement, which are bound to each other through sp^2 hybridization. Consequently, unique properties including high carrier mobility, half-integer quantum effects, high thermal conductivity, high mechanical stability, large specific surface area, and high chemical reactivity are originated.[2,3] However, one of the most important features of graphene is its zero energy gap, which represents a drawback for its electronic applications such as field-effect transistors because of its low ON/OFF ratio. A similar feature has been found for other well-known elemental 2D materials, such as silicene[4] and germanene.[5] Therefore, band-gap opening has been investigated, which can be achieved through edge engineering,[6,7] thickness engineering and heterostructure formation,[8,9] or chemical functionalization.[10,11] Moreover, the field of 2D materials has grown vastly with the discovery of new members beyond graphene; notable examples include transition metal dichalcogenides (TMDs),[12,13] hexagonal boron nitride (h-BN),[14,15] transition metal carbides/nitrides (MXenes),[16,17] and metal oxides,[18,19] among others. In addition, novel properties can be obtained by varying the thickness,[20,21] strain engineering,[22,23] defect engineering,[24,25] impurity doping,[26,27] and stacking two or more different 2D materials to form heterostructures.[28,29] Unique properties, superior to those of their bulk counterparts, have enabled 2D materials to show promise in

---

[a] *Faculty of Fundamental Sciences, Posts and Telecommunications Institute of Technology, Hanoi, Vietnam*

[b] *Center of Scientific Research and Application, Lac Hong University, No. 10 Huynh Van Nghe Str, Tran Bien Ward, Dong Nai Province, Vietnam*

[c] *Laboratory for Computational Physics, Institute for Computational Science and Artificial Intelligence, Van Lang University, Ho Chi Minh City, Vietnam*

[d] *Faculty of Mechanical, Electrical, and Computer Engineering, Van Lang School of Technology, Van Lang University, Ho Chi Minh City, Vietnam*

[e] *Universidad Nacional Autónoma de México, Centro de Nanociencias y Nanotecnología, Apartado Postal 14, Ensenada, Baja California, Código Postal 22800, Mexico*

[f] *Institute of Theoretical and Applied Research, Duy Tan University, Ha Noi 100000, Vietnam*

[g] *School of Engineering and Technology, Duy Tan University, Da Nang 550000, Vietnam. E-mail: dominhhoat@duytan.edu.vn*

diverse applications, including optoelectronics, photonics, and electronics,[30,31] photovoltaics,[32,33] catalysis,[34,35] energy production and storage,[36,37] and emergent spintronics,[38,39] among others.

Spintronics, or spin-based electronics, is an emerging form of electronics, which explores electron spin as an additional degree of freedom. Despite their promise for conventional electronic devices, the use of 2D materials for spintronics is greatly limited because most of them are intrinsically nonmagnetic (for examples, TMDs, hBN, and group-IV-based materials). Therefore, the ability to tune and manipulate spin states in 2D materials is of great importance from both fundamental scientific and technological point of views. In this regard, impurity doping is a well-accepted and widely employed method because of its simplicity, easy realization, and effectiveness in adjusting the intrinsic physical and chemical properties of 2D materials. For instance, doping with nonmetal atoms has been demonstrated to induce magnetic states in 2D nonmagnetic semiconductors. For example, first-principles calculations performed by Hernández-Tecorralco *et al.*[40] have confirmed magnetic moments of up to 1.0 μ_B in graphene doped with pnictogen atoms.[40] Theoretically, ferromagnetic half-metallicity has also been reported in a ZnO monolayer by B or C substitution, whereas doping with N, Si, and P atoms leads to ferromagnetic semiconducting behavior[41] Likewise, various nonmetal impurities have been predicted to induce magnetic states in TMD monolayers.[42,43] Therefore, nonmetal doping can be introduced as an effective method for engineering magnetism in 2D materials without the need for unpaired d or f electrons.

On the other hand, Zhong *et al.*[44] have successfully realized the physical vapour deposition (PVD) of a large-scale PbI_2 monolayer with high crystallinity. Photoluminescence characterization and first-principles calculations reveal that it is an indirect-gap semiconductor. This experimental work has aroused significant interest in 2D group-IV di-iodides.[45–48] In particular, a semiconductor SnI_2 monolayer has been successfully fabricated by Yuan *et al.*[49] using molecular beam epitaxy. Scanning tunneling microscopy/spectroscopy characterization indicates a band gap of ≈2.9 eV, which is also corroborated by density functional theory calculations. The SnI_2 monolayer is a promising candidate for optoelectronic devices because of its excellent light absorption in the visible and ultraviolet regimes.[50,51] Moreover, its ultralow lattice thermal conductivity also makes this 2D material promising for thermoelectric applications.[52,53] However, the exploration of the SnI_2 monolayer as a 2D platform for spintronic applications is still lacking.

To the best of our knowledge, changing the physical properties of the SnI_2 monolayer by doping with nonmetal atoms has not been investigated. In this work, we propose pnictogen (X = P and As) doping to functionalize the SnI_2 monolayer in order to introduce new functionalities to this 2D material. This choice originates from the different valence electronic configurations of P/As atoms and I atom, which may create hole (p-doping) in the SnI_2 monolayer. Our first-principles calculations confirm that the bare SnI_2 monolayer is nonmagnetic, while P and As substitution induces magnetic states in this monolayer, along with either half-metallic or magnetic semiconductor characteristics suitable for spintronic applications. In addition, we also investigate the magnetic coupling and magnetic anisotropy that will be useful for recommending the doped SnI_2 systems for practical applications, including magnetoresistive random-access memory (MRAM) fabrication, magnetic-field sensing, and spin-current generation.

2. Computational details

Within the framework of density functional theory (DFT),[54] the projector augmented wave (PAW) method and the Perdew–Burke–Ernzerhof-parameterised generalized gradient approximation (GGA-PBE)[55] are adopted to investigate the electronic and magnetic properties of pristine and doped SnI_2 monolayers. It is important to mention that the GGA-PBE functional generally underestimates the material band gap. To overcome this limitation, hybrid functionals incorporating a fraction of the exact Hartree exchange potential have been proposed to provide accurate band-gap predictions—for example, the HSE06 functional with a 25% fraction of the Hartree exchange potential.[56] However, the PBE functional is employed in this work because it describes very well the band structure profile, providing reliable results for the variation of electronic and magnetic properties upon doping. Weak van der Waals interactions are treated using the DFT-D3 method with the zero-damping function proposed by Grimme *et al.*[57] All calculations are performed using the Vienna *ab initio* simulations (VASP) package.[58,59] The valence electronic configurations of the constituent elements are as follows: Sn-$5s^25p^2$, I-$5s^25p^5$, P-$3s^23p^3$, and As-$4s^24p^3$. The wave functions are expanded using a plane-wave basis set with a cutoff energy of 500 eV. The criterion of energy convergence for the self-consistent calculations is set to 1×10^{-6} eV. The structures are relaxed until the residual force is less than 1×10^{-2} eV Å^{-1} to obtain the optimal geometry. The Brillouin zones are sampled using Monkhorst–Pack *k*-point grids.[60] Specifically, a 20 × 20 × 1 mesh is applied to the SnI_2 monolayer unit cell. In all cases, the structural models are built with a vacuum thickness greater than 15 Å along the perpendicular (*z*-axis) direction to minimize the spurious interactions between neighboring image layers.

To simulate the doping, a 4 × 4 × 1 supercell is generated, in which P/As atoms substitute the host I atoms. This supercell is large enough to minimize the interactions between the impurities and their periodic images. In these cases, the Brillouin zone is integrated with a Monkhorst–Pack *k*-point grid of 4 × 4 × 1. To estimate the energy required to realize the doping processes, the formation energy E_f is computed using the following expression:

$$E_{\mathrm{f}} = \frac{E(n\mathrm{X@SI2}) - E(\mathrm{SI2}) + n\mu_{\mathrm{I}} - n\mu_{\mathrm{X}}}{n}, \quad (1)$$

where $E(n\mathrm{X@SI2})$ and $E(\mathrm{SI2})$ are the total energies of the *n*X-doped and bare SnI_2 monolayers (X = P and As), respectively; *n* is the number of impurities; and μ_{I} and μ_{X} denote the chemical potentials of the I and X atoms, respectively. To examine the stability of the doped SnI_2 systems, their cohesive energy E_c is determined as follows:

$$E_c = \frac{E(n\mathrm{X@SI2}) - 16E(\mathrm{Sn}) - (32-n)E(\mathrm{I}) - nE(\mathrm{X})}{48}, \tag{2}$$

where $E(\mathrm{Sn})$, $E(\mathrm{I})$, and $E(\mathrm{X})$ refer to the energies of isolated Sn, I, and X atoms, respectively.

In order to suggest practical applications, the magnetic anisotropy should be determined, as it is essential for the storage of magnetic information. For such a goal, the magnetic anisotropy energy (MAE) is calculated as

$$\mathrm{MAE} = E[100] - E[001]. \tag{3}$$

$E[100]$ and $E[001]$ are the total energies calculated using a two-step approach: (1) self-consistent calculations without spin–orbit coupling (SOC) to obtain the charge density, followed by (2) non-self-consistent calculations with SOC, with the magnetization constrained along the [100] and [001] crystallographic directions, respectively. The MAE provides information into the preferred magnetization direction. Specifically, negative MAE values indicate in-plane magnetic anisotropy (IMA) since the monolayer systems are expanded in the *xy*-plane, while positive MAE values correspond to perpendicular magnetic anisotropy (PMA).

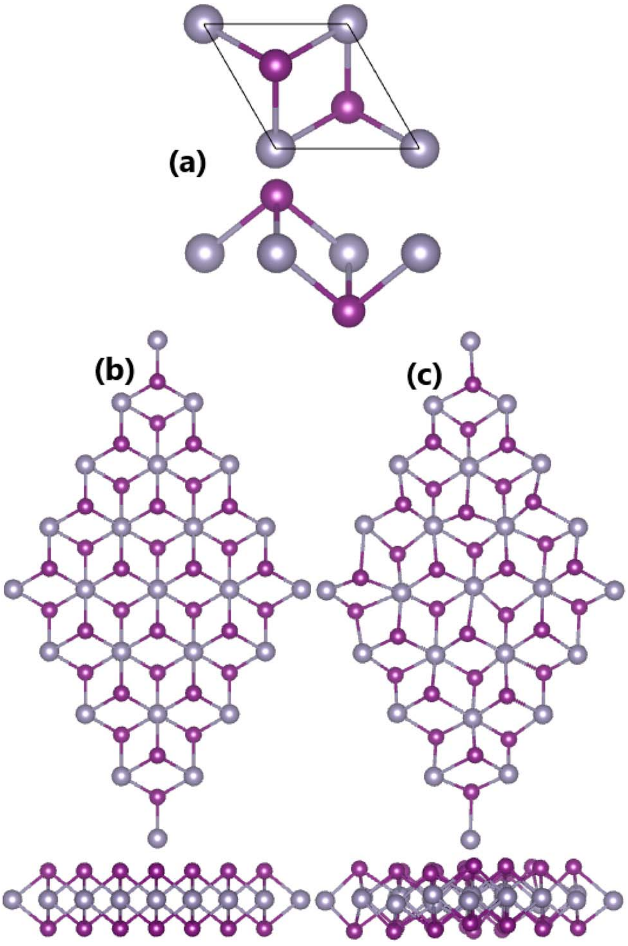

Fig. 1 Atomic structure of the SnI_2 monolayer visualized in (a) a unit cell, (b) a 4 × 4 × 1 supercell at equilibrium, and (c) a 4 × 4 × 1 supercell after 10 ps of AIMD simulations (grey spheres: Sn atoms; violet spheres: I atoms).

3. Results and discussion

3.1. Structural and electronic properties of the SnI_2 monolayer

Fig. 1a shows the optimized atomic structure of the SnI_2 monolayer in a unit cell, while its 4 × 4 × 1 supercell is displayed in Fig. 1b. The atomic stacking follows an I–Sn–I sequence. The structure belongs to the $P\bar{3}m1$ space group (no. 164). Each unit cell contains one SnI_2 formula unit, consisting of one Sn atom and two I atoms, with the following structural parameters: (1) lattice constant a = 4.58 Å; (2) chemical bond length $d_{\mathrm{Sn-I}} = 3.22$ Å; (3) interatomic angles $\angle\mathrm{SnISn} = 90.70°$ and $\angle\mathrm{ISnI} = 89.30°$; and (4) monolayer thickness $\Delta = 2 \times \Delta_{\mathrm{Sn-I}} = 2 \times 1.84 = 3.68$ Å. These structural parameters are in good agreement with previous studies,[52] where a negligible deviation of only 0.22% in the lattice constant is presented. Once optimized, we analyze the stability of the SnI_2 monolayer using the following criteria:

- The dynamical stability is determined by calculating phonon dispersive spectra using the PHONOPY code.[61] A 4 × 4 × 1 supercell is considered, and the finite displacement method is adopted. Fig. 2a shows the calculated phonon spectra of the SnI_2 monolayer, which consist of nine phonon modes (including three acoustic modes and six optical modes. Our calculations assert that there are no nonphysical imaginary frequencies in the whole Brillouin zone. This means that the SnI_2 monolayer is dynamically stable.
- *Ab initio* molecular dynamics (AIMD) simulations in the canonical ensemble (constant number, volume, and temperature) are carried out, lasting for 10 ps with a time step of 2 fs

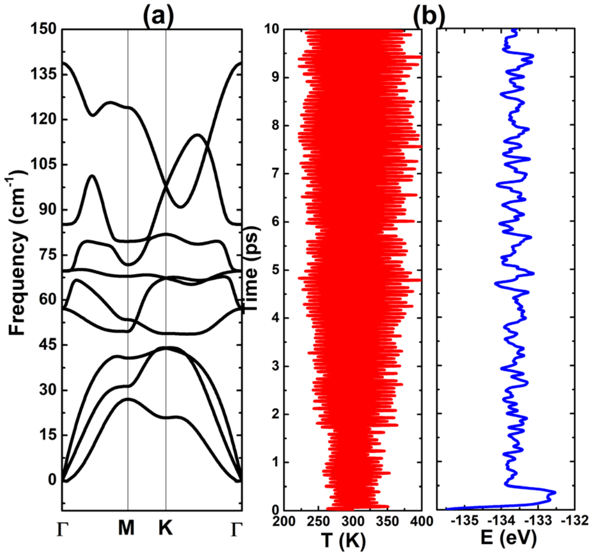

Fig. 2 (a) Phonon dispersion spectra and (b) fluctuations of temperature and energy during the AIMD simulations of the SnI_2 monolayer.

(5000 simulation steps). The Nosé–Hoover thermostat[62,63] is employed. A 4 × 4 × 1 supercell is constructed to minimize the effects of periodic boundary conditions. From Fig. 1b, it can be seen that the SnI_2 monolayer maintains its structural integrity after heating to 300 K; no chemical bonds are broken since the constituent atoms only exhibit small movements from their equilibrium sites. In addition, temperature and energy slightly fluctuate around their equilibrium values during the simulation period, as observed in Fig. 2b, where the fluctuations remain within a small range of ±5%. From these results, it is safe to confirm that the SnI_2 monolayer is thermally stable.

- Mechanical stability is further assessed using two independent elastic constants C_{11} and C_{12}, which should satisfy the Born criteria for the stability of 2D hexagonal symmetry:[64] $C_{11} > 0$ and $C_{11} > |C_{12}|$. In our case, the calculated values of C_{11} and C_{12} are 16.029 and 3.893 N m^{-1}, respectively. Since the Born criteria are satisfied, it can be concluded that the SnI_2 monolayer is mechanically stable. In addition, Young's modulus Y and Poisson's ratio γ are derived from elastic constants as follows:[65] $Y = \frac{{C_{11}}^2 - {C_{12}}^2}{C_{11}}$ and $\gamma = \frac{C_{12}}{C_{11}}$. For the SnI_2 monolayer, Young's modulus is calculated to be 15.08 N m^{-1}, which is much smaller than that of graphene (335 N m^{-1}),[66] h-BN (331 N m^{-1}),[67] and MoS_2 (119 N m^{-1}).[68] These results indicate that the SnI_2 monolayer possesses low mechanical strength, which should be considered when designing potential applications. Moreover, the Poisson's ratio of this monolayer is 0.24, which is comparable to those of graphene, h-BN, and MoS_2.

The orbital-decomposed band structure of the SnI_2 monolayer is shown in Fig. 3a. The calculated band structure confirms the indirect-gap semiconducting nature of the SnI_2 monolayer, in which the highest point of the valence band is located along the Γ–K path and the lowest point of the conduction band appears at the Γ point. According to our calculations, this 2D material has a band gap of 2.03 eV, which is consistent with previous reports.[69] By including spin–orbit coupling (SOC), an energy gap of 1.88 eV is obtained at the PBE+SOC theoretical level (see Fig. S3 of the SI file). Our results are smaller than the experimental band gap (~2.9 eV)[49] as a consequence of the band gap underestimation of the GGA-PBE functional. Note that hybridized Sn-s and I-$p_{x,y,z}$ states form the upper valence band, while the lower conduction band part is formed mainly by the Sn-p_z state. In the considered energy range, I-$p_{x,y,z}$ and Sn-$p_{x,y,z}$ states also construct the lower

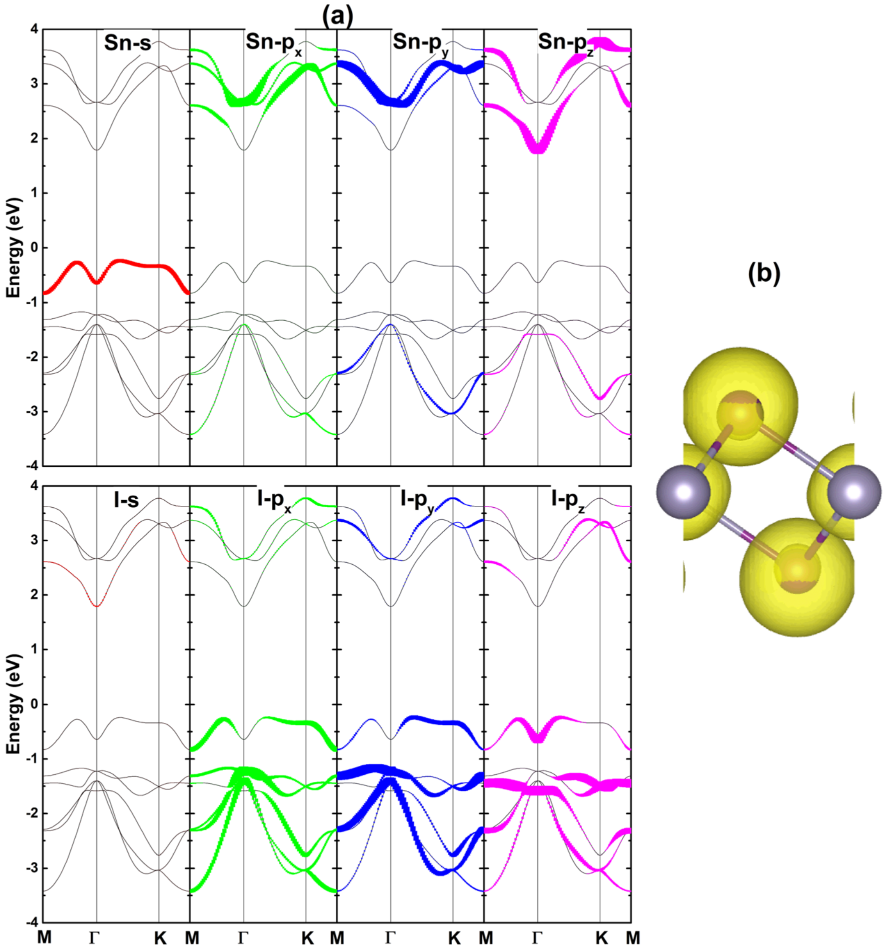

Fig. 3 (a) Orbital-decomposed band structure (the Fermi level is set to 0 eV) and (b) electron localization function (iso-surface value: 0.8 e Å^{-3}) of the SnI_2 monolayer.

valence band and upper conduction band, respectively. The Sn-s/I-$p_{x,y,z}$ hybridization may produce the covalent character of the Sn–I bond, which is further confirmed by the charge distributed in the interatomic regions (see Fig. 3b). However, the difference in electronegativity between Sn and I atoms also leads to charge transfer, which is further studied quantitatively using Bader charge analysis. It is found that each Sn atom transfers 0.90 e to of charge to the I atoms (each I atom attracts 0.45 e). The same feature has been found in a PbI_2 monolayer, in which each I atom attracts 0.4 e from a Pb atom.[70] These results demonstrate that the Sn–I chemical bond has both covalent and ionic character.

3.2. Effects of single pnictogen impurity

In this section, the effects of pnictogen impurities on the SnI_2 monolayer's electronic and magnetic properties are investigated, where one pnictogen (X = P and As) atom substitutes one I atom in a 4 × 4 × 1 supercell. The single-atom-doped SnI_2 systems are denoted as 1X@SI2. Our calculated formation energies indicate energy costs of 3.15 and 2.87 eV per atom to realize the P and As doping processes, respectively. Moreover, the 1P@SI2 and 1As@SI2 systems exhibit negative E_c values of −2.57 eV per atom, which suggests their good structural and chemical stability. It is worth noting that the cohesive energy of the SnI_2 monolayer (calculated to be −2.59 eV per atom) varies insignificantly upon doping, indicating negligible effects on the structural and chemical stability of this 2D material. The optimized atomic structures of the 1P@SI2 and 1As@SI2 systems are given in Fig. S1 of the SI file. From the structural relaxation, the chemical bond lengths $d_{\text{P–Sn}}/d_{\text{As–Sn}}$ and buckling heights $\Delta_{\text{P–Sn}}/\Delta_{\text{As–Sn}}$ are calculated to be 2.65/2.77 and 1.35/1.51 Å, respectively. Note that these values are smaller than those of the pristine monolayer ($d_{\text{I–Sn}}$ and $\Delta_{\text{I–Sn}}$), indicating a local contraction of the SnI_2 monolayer caused by pnictogen impurities. This structural distortion can be attributed to the smaller atomic sizes of P/As atoms in comparison with that of an I atom.

The ionic interactions between pnictogen impurities and their neighboring atoms in SnI_2 monolayer are analyzed through charge density difference $\Delta\rho$ calculated as

$$\Delta\rho = \rho(\text{1X@SI2}) - \rho(\text{SI2}) - \rho(\text{1X}), \tag{4}$$

where ρ(1X@SI2), ρ(SI2), and ρ(1X) are the charge densities of the 1X@SI2 system, the bare SnI_2 monolayer, and a single X atom, respectively, and are computed using self-consistent calculations. As illustrated in Fig. 4a and c, charge accumulation at the P and As sites is visualized by yellow iso-surfaces, while their nearest neighboring Sn atoms exhibit charge depletion that is visualized by aqua iso-surfaces. This feature originates from the ability of pnictogen atoms to attract charge due to their greater electronegativity compared with Sn atoms. The ionic interactions originating from this charge transfer are quantitatively studied using Bader charge analysis. It is found that P and As impurities attract charge amounts of 0.63 and 0.45 e from the host SnI_2 monolayer, respectively. Note that the P atom gains a larger quantity because it is more electronegative than the As atom. The charge density in 1X-doped SnI_2 monolayer systems is visualized in Fig. S4 of the SI file, which shows significant redistribution around the doping sites.

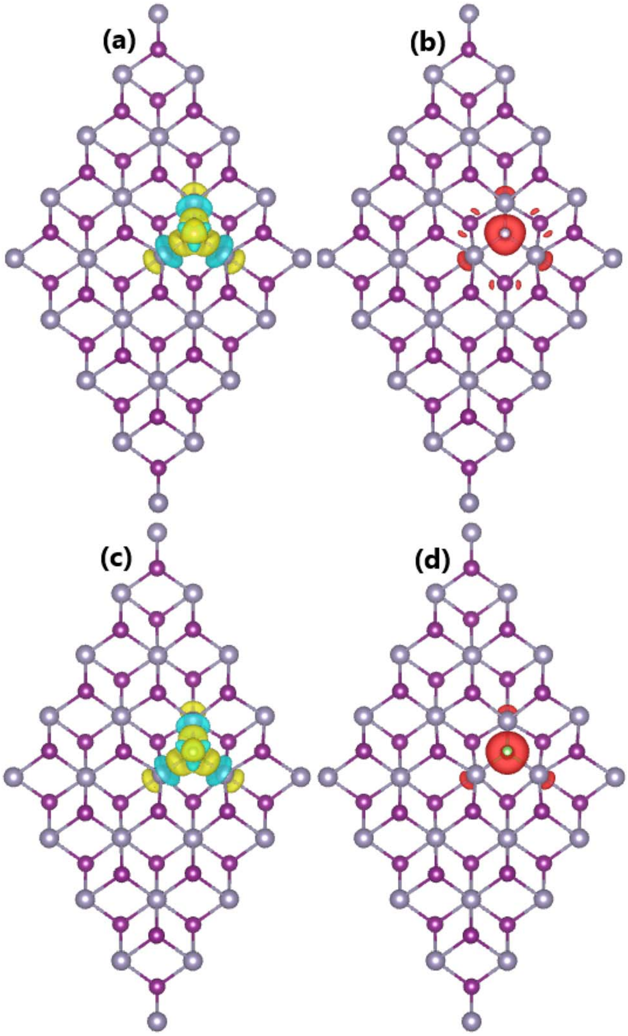

Fig. 4 Charge density difference (iso-surface value: 0.002 e Å^{-3}; yellow iso-surface: charge enrichment; aqua iso-surface: charge depletion) and spin density (iso-surface value: 0.005 e Å^{-3}) of (a and b) 1P- and (c and d) 1As-doped SnI_2 monolayers.

Our spin-polarized calculations confirm the presence of magnetic states in the 1P@SI2 and 1As@SI2 systems, with each exhibiting an overall magnetic moment of 2.00 μ_B. The spin density is further evaluated to analyze the atomic contributions to the magnetic moment. From the results visualized in Fig. 4b and d, one can see large spin iso-surfaces centered mainly at the doping sites, indicating the key role of the pnictogen (X) impurities in generating the magnetic properties of the 1X@SI2 systems. Moreover, a small contribution from the nearest-neighbor Sn atoms is also observed. In addition, the magnetic anisotropy energy of the 1P@SI2 and 1As@SI2 systems is calculated to be −2482.23 and −934.4 μeV per supercell. Negative MAE values indicate the IMA of both systems, suggesting their potential for magnetic-field-sensing applications. Note that the 1P@SI2 monolayer exhibits stronger in-plane magnetic anisotropy considering its significantly more negative MAE value compared to the 1As@SI2 monolayer. This difference can be attributed to the strong orbital hybridization and mixing of the in-plane $p_{x,y}$ states of the P–Sn interactions.

The doping-induced magnetic states in the SnI_2 monolayer are also reflected in the calculated spin-resolved band structures and projected density of states (PDOS) of the pnictogen impurities and their nearest neighboring Sn atoms in the 1X@SI2 systems, as shown in Fig. 5. From the figure, strong spin polarization can be observed, generated by new mid-gap energy subbands in the vicinity of the Fermi level, whose flat form indicates their origin from the localized states. The spin-up state of the 1P@SI2 and 1As@SI2 systems has indirect gaps of 1.81 and 1.74 eV, respectively. Note that these values are determined by the separation between the flat energy band below the Fermi level—originating mainly from P/As-$p_{x,y,z}$ and Sn-s states—and the lower conduction band, which is formed mainly by Sn-$p_{x,y,z}$ states. Meanwhile, very small band gaps of 0.09 and 0.05 eV are obtained for the spin-down state of the 1P@SI2 and 1As@SI2 systems, respectively. These small values can be attributed to the mid-gap flat subbands located close to each other: one below the Fermi level, formed mainly by P/As-p_z states, and the other above the Fermi level, built primarily from P/As-$p_{x,y}$ states. This analysis demonstrates the importance of P-3p and As-4p orbitals in regulating the magnetic semiconductor nature of 1P@SI2 and 1As@SI2 systems, respectively. It is worth noting that the spin-down state could be metallized under the effects of external factors, such as thermal fluctuations, because of its very small band gap. Consequently, the 1P@SI2 and 1As@SI2 systems could become half-metallic, offering potential for additional functionality.

3.3. Study of spin coupling

Now, the magnetic phase of the P- and As-doped SnI_2 monolayers is determined by examining the spin coupling between pnictogen impurities. For such a goal, two pnictogen X impurities replace two I atoms in a 4 × 4 × 1 supercell. For each impurity type, two doping configurations are considered, and

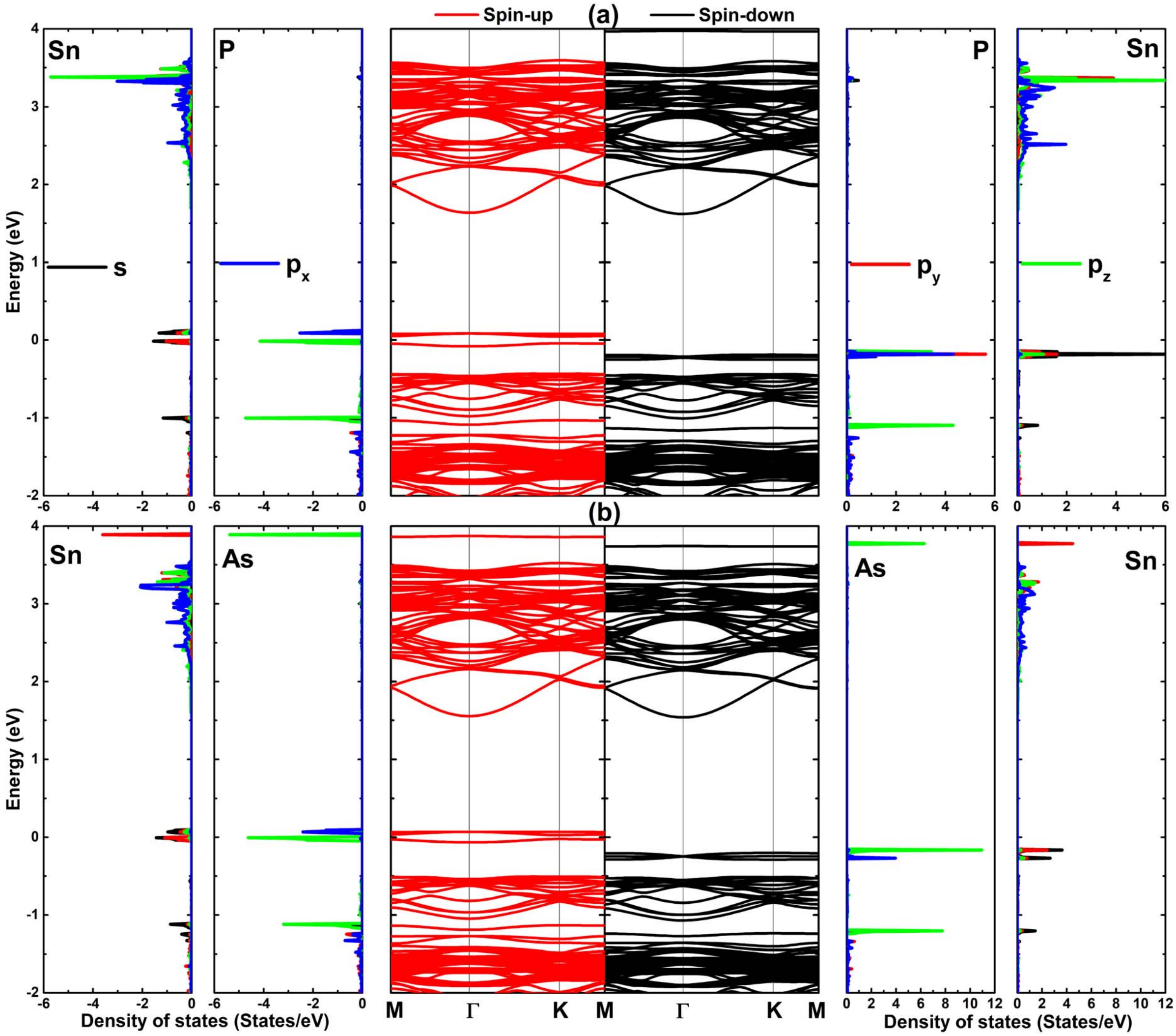

Fig. 5 Spin-resolved band structure and projected density of states (pnictogen impurities and their nearest neighboring Sn atoms) of (a) 1P- and (b) 1As-doped SnI_2 monolayers (the Fermi level is set to 0 eV).

the doped systems are denoted as 2X-1@SI2 and 2X-2@SI2, where the separation between the X atoms increases from 2X-1 to 2X-2 doping configurations (see the optimized atomic structure visualized in Fig. S2 of the SI file). Specifically, the inter-dopant separation is 4.52 and 4.74 Å in 2P-1@SI2 and 2As-1@SI2 systems, respectively. In the cases of 2P-2@SI2 and 2As-2@SI2 systems, the separation is 9.16 Å. In the previous subsection, it was confirmed that the system magnetism is mainly produced by the pnictogen impurities. Therefore, the constrained local magnetic moments of the X atoms are initially set to be parallel to simulate the ferromagnetic (FM) phase, while the antiferromagnetic (AFM) phased is modeled with an antiparallel configuration. Fig. 6 shows the spin densities of the 2X-1@SI2 and 2X-2@SI2 systems, as well as the energy of the magnetic phase transitions. According to our calculations, a small X–X separation induces the AFM phase, which exhibits a smaller energy than the FM phase. In these cases, the energy difference for the 2P-1@SI2 and 2As-1@SI2 systems is 32.41 and 34.74 meV, respectively. The AFM-to-FM phase transition is induced by further separating the pnictogen impurities, such that parallel spin coupling is energetically favorable in the 2P-2@SI2 and 2As-2@SI2 systems with energy differences of 72.92 and 119.55 meV, respectively. For these ferromagnetic systems, the Curie temperature T_C is computed using the mean-field approximation as follows:

$$T_C = \frac{-2\Delta E}{3Nk_B}, \tag{5}$$

where ΔE refers to the energy difference between the FM and AFM states; k_B is the Boltzmann constant; and $N = 2$ is the number of pnictogen impurities in the supercell. According to our calculations, T_C values of 282.20 and 462.66 K are obtained

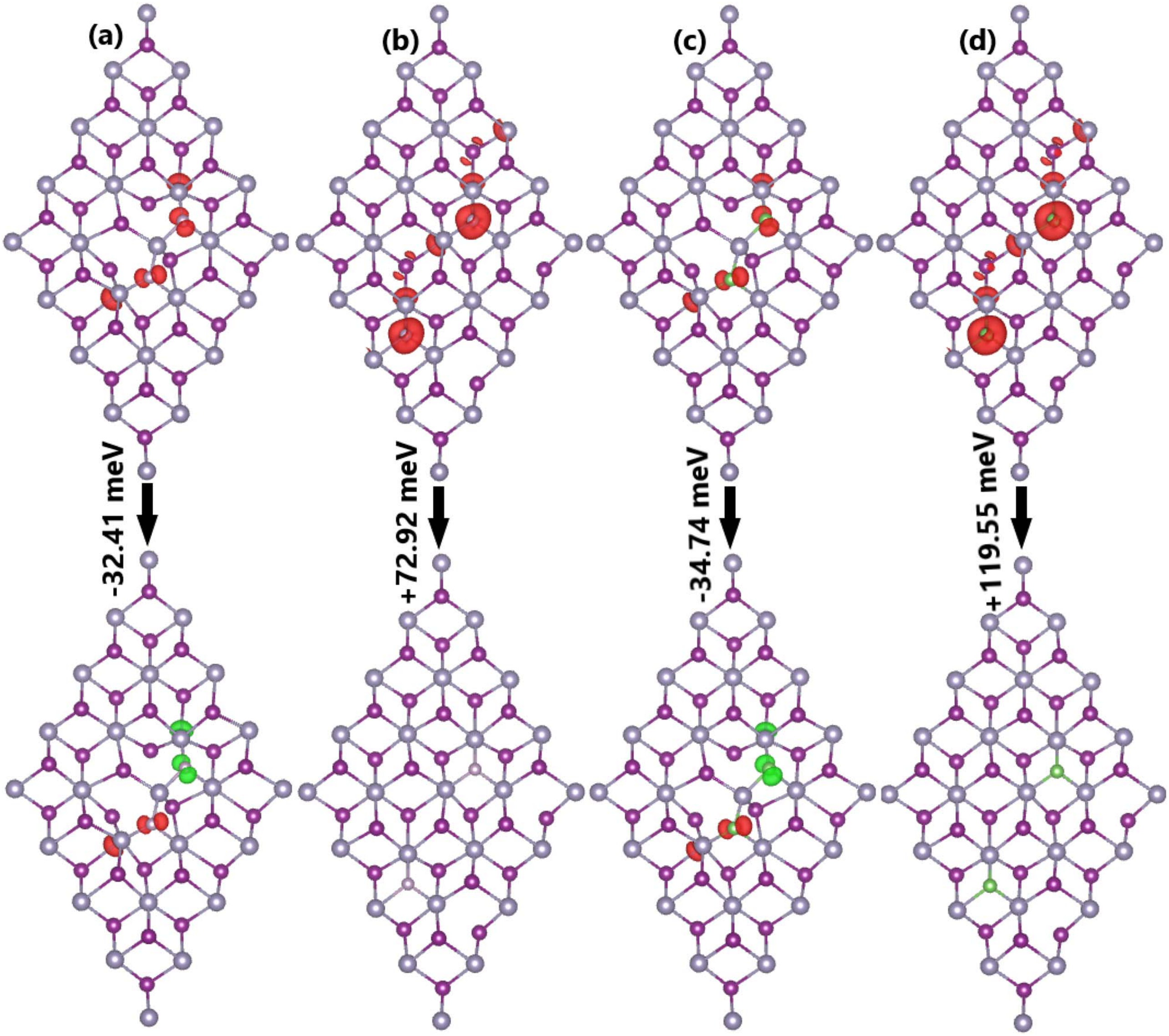

Fig. 6 Spin density and magnetic-phase transition energies of (a) 2P-1-, (b) 2P-2-, (c) 2As-1-, and (d) 2As-2-doped SnI_2 monolayers (iso-surface value: 0.005 e Å^{-3}; red iso-surface: positive spin value; green iso-surface: negative spin value; top row: parallel spin coupling was initially set; bottom row: antiparallel spin coupling was initially set).

for the 2P-2@SI2 and 2As-2@SI2 systems, respectively. Large Curie temperatures suggest good robustness of the ferromagnetism in the SnI_2 monolayer induced by pnictogen impurities. In addition, the X–X separation also induces the PMA-to-IMA switching of the magnetic anisotropy. Specifically, the magnetic anisotropy energy of the 2P-1@SI2 and 2As-1@SI2 systems is calculated to be 257.7 and 10 539.21 μeV per supercell, respectively, indicating perpendicular magnetic anisotropy. Note that the PMA of the 2As-1@SI2 system is quite strong, as suggested by its large MAE value. A large X–X interatomic distance induces in-plane magnetic anisotropy in the 2P-2@SI2 and 2As-2@SI2 systems with negative MAE values of −2393.20 and −1278.22 μeV per supercell, respectively. These results suggest an efficient approach to selectively design applications for the pnictogen-doped SnI_2 monolayer, such as for MRAM fabrication (with PMA required) and magnetic field sensing (with IMA required).

Fig. 7 shows the spin-resolved band structures of the 2X-1@SI2 systems in the AFM phase and the 2X-2@SI2 systems in the FM phase, whose electronic nature is determined by the flat mid-gap energy states. It can be noted that the 2P-1@SI2 and 2As-1@SI2 systems exhibit an antiferromagnetic semiconducting nature with energy gaps of 0.27 and 0.26 eV, respectively, where no spin polarization is observed since spin states are symmetric. In contrast, the 2P-2@SI2 and 2As-2@SI2 systems exhibit strong spin polarization around the Fermi level. The semiconductor spin-up state with an indirect energy gap of 1.68 eV and the metallic spin-down state give rise to the formation of ferromagnetic half-metallicity in the 2P-2@SI2 system. Conversely, the 2As-2@SI2 system shows semiconducting behavior for both the spin-up and spin-down states, with indirect gaps of 1.65 and 0.11 eV, respectively, confirming the emergence of the ferromagnetic semiconducting nature that can be attributed to the orbital overlap and hybridization between As impurities and their neighboring atoms as a result of the larger atomic radius of the As atom compared to the P atom.

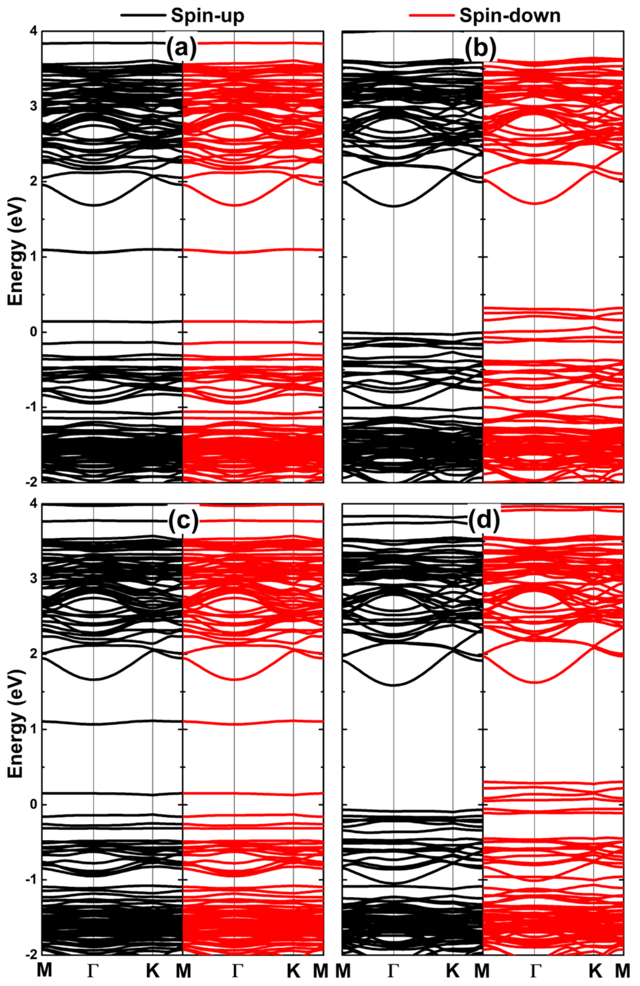

Fig. 7 Spin-resolved band structure of (a) 2P-1-, (b) 2P-2-, (c) 2As-1-, and (d) 2As-2-doped SnI_2 monolayers (the Fermi level is set to 0 eV).

4. Conclusions

In summary, first-principles calculations have been performed to systematically investigate the effects of pnictogen (X = P and As) doping on the electronic and magnetic properties of the SnI_2 monolayer. Good stability is confirmed for the pristine SnI_2 monolayer, which is a 2D indirect-gap semiconductor whose band gap originates mainly from the hybridization between Sn-s and I-$p_{x,y,z}$ states. This electronic hybridization gives rise to the covalent character of the Sn–I chemical bond, while the ionic character is a result of the charge transfer from the less electronegative Sn atom to the more electronegative I atom. Once incorporated into the SnI_2 monolayer lattice, P and As impurities attract charge from the host monolayer. Interestingly, spin states with in-plane magnetic anisotropy are also induced by pnictogen doping, primarily generated by the impurities. The interactions between X-$p_{x,y,z}$ and Sn-s states form new mid-gap subbands that give rise to magnetic semiconducting behavior. Our study also reveals interesting electronic and magnetic properties controlled by the X–X separation. An antiferromagnetic semiconducting nature with perpendicular magnetic anisotropy is obtained when the X impurities are close to each other. Increasing their separation leads to the formation of new 2D materials that are ferromagnetic half-metals (for P doping) or ferromagnetic semiconductors (for As doping). Moreover, the magnetic anisotropy is switches from PMA to IMA. High Curie temperatures of 282.20 and 462.66 K are obtained by P and As doping, respectively. Thus, controlling the inter-dopant separation can be employed to regulate the electronic and magnetic properties of doped SnI_2 monolayer systems when designing new functional 2D materials. Our results demonstrate that pnictogen doping is an effective functionalization method for inducing d^0 magnetism in the nonmagnetic SnI_2 monolayer, which exhibits feature-rich electronic and magnetic properties suitable for selective spintronic applications.

Conflicts of interest

The authors declare that they have no known competing financial interests or personal relationships that could have appeared to influence the work reported in this paper.

Data availability

Data will be provided upon request to the authors.

Supplementary information (SI): atomic structure and charge density of the doped SnI_2 monolayer systems are given. In addition, the band structure with SOC of pristine monolayer is also presented. See DOI: https://doi.org/10.1039/d5ra09400c.

Acknowledgements

Calculations were performed in DGCTIC-UNAM Supercomputing Center (projects LANCAD-UNAM-DGTIC-368).

References

1 K. S. Novoselov, A. K. Geim, S. V. Morozov, D.-e. Jiang, Y. Zhang, S. V. Dubonos, I. V. Grigorieva and A. A. Firsov, Electric field effect in atomically thin carbon films, *Science*, 2004, **306**(5696), 666–669.

2 C. Soldano, A. Mahmood and E. Dujardin, Production, properties and potential of graphene, *Carbon*, 2010, **48**(8), 2127–2150.

3 D. R. Cooper, B. D'Anjou, N. Ghattamaneni, B. Harack, M. Hilke, A. Horth, N. Majlis, M. Massicotte, L. Vandsburger, E. Whiteway, *et al.*, Experimental review of graphene, *Int. Scholarly Res. Not.*, 2012, **2012**(1), 501686.

4 A. Kara, H. Enriquez, A. P. Seitsonen, L. L. Y. Voon, S. Vizzini, B. Aufray and H. Oughaddou, A review on silicene—new candidate for electronics, *Surf. Sci. Rep.*, 2012, **67**(1), 1–18.

5 A. Acun, L. Zhang, P. Bampoulis, M. v. Farmanbar, A. van Houselt, A. Rudenko, M. Lingenfelder, G. Brocks, B. Poelsema, M. Katsnelson, *et al.*, Germanene: the germanium analogue of graphene, *J. Phys. Condens. Matter*, 2015, **27**(44), 443002.

6 A. Pandya, K. Sangani and P. K. Jha, Band gap determination of graphene, h-boron nitride, phosphorene, silicene, stanene, and germanene nanoribbons, *J. Phys. D: Appl. Phys.*, 2020, **53**(41), 415103.

7 S. Kaneko, H. Tsuchiya, Y. Kamakura, N. Mori and M. Ogawa, Theoretical performance estimation of silicene, germanene, and graphene nanoribbon field-effect transistors under ballistic transport, *Appl. Phys. Express*, 2014, **7**(3), 035102.

8 C. H. Lui, Z. Li, K. F. Mak, E. Cappelluti and T. F. Heinz, Observation of an electrically tunable band gap in trilayer graphene, *Nat. Phys.*, 2011, **7**(12), 944–947.

9 R. M. Torres-Rojas, D. A. Contreras-Solorio, L. Hernández and A. Enciso, Band gap variation in bi, tri and few-layered 2D graphene/hBN heterostructures, *Solid State Commun.*, 2022, **341**, 114553.

10 N. Liu, G. Bo, Y. Liu, X. Xu, Y. Du and S. X. Dou, Recent progress on germanene and functionalized germanene: preparation, characterizations, applications, and challenges, *Small*, 2019, **15**(32), 1805147.

11 T. Kuila, S. Bose, A. K. Mishra, P. Khanra, N. H. Kim and J. H. Lee, Chemical functionalization of graphene and its applications, *Prog. Mater. Sci.*, 2012, **57**(7), 1061–1105.

12 S. Manzeli, D. Ovchinnikov, D. Pasquier, O. V. Yazyev and A. Kis, 2D transition metal dichalcogenides, *Nat. Rev. Mater.*, 2017, **2**(8), 17033.

13 S. Joseph, J. Mohan, S. Lakshmy, S. Thomas, B. Chakraborty, S. Thomas and N. Kalarikkal, A review of the synthesis, properties, and applications of 2D transition metal dichalcogenides and their heterostructures, *Mater. Chem. Phys.*, 2023, **297**, 127332.

14 A. E. Naclerio and P. R. Kidambi, A review of scalable hexagonal boron nitride (h-BN) synthesis for present and future applications, *Adv. Mater.*, 2023, **35**(6), 2207374.

15 L. Li, Y. Zhang, R. Zhang, Z. Han, H. Dong, G. Yu, D. Geng and H. Y. Yang, A minireview on chemical vapor deposition growth of wafer-scale monolayer h-BN single crystals, *Nanoscale*, 2021, **13**(41), 17310–17317.

16 Y. Wei, P. Zhang, R. A. Soomro, Q. Zhu and B. Xu, Advances in the synthesis of 2D MXenes, *Adv. Mater.*, 2021, **33**(39), 2103148.

17 D. Ayodhya, A review of recent progress in 2D MXenes: Synthesis, properties, and applications, *Diamond Relat. Mater.*, 2023, **132**, 109634.

18 K. Zhou, G. Shang, H.-H. Hsu, S.-T. Han, V. A. Roy and Y. Zhou, Emerging 2D metal oxides: from synthesis to device integration, *Adv. Mater.*, 2023, **35**(21), 2207774.

19 P. Kumbhakar, C. C. Gowda, P. L. Mahapatra, M. Mukherjee, K. D. Malviya, M. Chaker, A. Chandra, B. Lahiri, P. Ajayan, D. Jariwala, *et al.*, Emerging 2D metal oxides and their applications, *Mater. Today*, 2021, **45**, 142–168.

20 X.-L. Li, W.-P. Han, J.-B. Wu, X.-F. Qiao, J. Zhang and P.-H. Tan, Layer-number dependent optical properties of 2D materials and their application for thickness determination, *Adv. Funct. Mater.*, 2017, **27**(19), 1604468.

21 K. Synnatschke, P. A. Cieslik, A. Harvey, A. Castellanos-Gomez, T. Tian, C.-J. Shih, A. Chernikov, E. J. Santos, J. N. Coleman and C. Backes, Length-and thickness-dependent optical response of liquid-exfoliated transition metal dichalcogenides, *Chem. Mater.*, 2019, **31**(24), 10049–10062.

22 G. G. Naumis, S. Barraza-Lopez, M. Oliva-Leyva and H. Terrones, Electronic and optical properties of strained graphene and other strained 2d materials: a review, *Rep. Prog. Phys.*, 2017, **80**(9), 096501.

23 S. Yang, Y. Chen and C. Jiang, Strain engineering of two-dimensional materials: Methods, properties, and applications, *InfoMat*, 2021, **3**(4), 397–420.

24 M. Tripathi, F. Lee, A. Michail, D. Anestopoulos, J. G. McHugh, S. P. Ogilvie, M. J. Large, A. A. Graf, P. J. Lynch, J. Parthenios, *et al.*, Structural defects modulate electronic and nanomechanical properties of 2D materials, *ACS Nano*, 2021, **15**(2), 2520–2531.

25 Z. Lin, B. R. Carvalho, E. Kahn, R. Lv, R. Rao, H. Terrones, M. A. Pimenta and M. Terrones, Defect engineering of two-dimensional transition metal dichalcogenides, *2D Materials*, 2016, **3**(2), 022002.

26 K. Zhang and J. Robinson, Doping of two-dimensional semiconductors: a rapid review and outlook, *MRS Adv.*, 2019, **4**(51–52), 2743–2757.

27 H. Yoo, K. Heo, M. H. R. Ansari and S. Cho, Recent advances in electrical doping of 2D semiconductor materials: Methods, analyses, and applications, *Nanomaterials*, 2021, **11**(4), 832.

28 K. S. Novoselov, A. Mishchenko, A. Carvalho and A. Castro Neto, 2D materials and van der Waals heterostructures, *Science*, 2016, **353**(6298), aac9439.

29 P. V. Pham, S. C. Bodepudi, K. Shehzad, Y. Liu, Y. Xu, B. Yu and X. Duan, 2D heterostructures for ubiquitous electronics and optoelectronics: principles, opportunities, and challenges, *Chem. Rev.*, 2022, **122**(6), 6514–6613.

30 J. S. Ponraj, Z.-Q. Xu, S. C. Dhanabalan, H. Mu, Y. Wang, J. Yuan, P. Li, S. Thakur, M. Ashrafi, K. Mccoubrey, *et al.*, Photonics and optoelectronics of two-dimensional materials beyond graphene, *Nanotechnology*, 2016, **27**(46), 462001.

31 J. Shim, H.-Y. Park, D.-H. Kang, J.-O. Kim, S.-H. Jo, Y. Park and J.-H. Park, Electronic and optoelectronic devices based on two-dimensional materials: From fabrication to application, *Adv. Electron. Mater.*, 2017, **3**(4), 1600364.

32 L. Wang, L. Huang, W. C. Tan, X. Feng, L. Chen, X. Huang and K.-W. Ang, 2D photovoltaic devices: progress and prospects, *Small Methods*, 2018, **2**(3), 1700294.

33 S. Das, D. Pandey, J. Thomas and T. Roy, The role of graphene and other 2D materials in solar photovoltaics, *Adv. Mater.*, 2019, **31**(1), 1802722.

34 L. Zhao, B. Wang and R. Wang, A critical review on new and efficient 2D materials for catalysis, *Adv. Mater. Interfaces*, 2022, **9**(29), 2200771.

35 T. A. Shifa, F. Wang, Y. Liu and J. He, Heterostructures based on 2D materials: a versatile platform for efficient catalysis, *Adv. Mater.*, 2019, **31**(45), 1804828.

36 B. Mendoza-Sánchez and Y. Gogotsi, Synthesis of two-dimensional materials for capacitive energy storage, *Adv. Mater.*, 2016, **28**(29), 6104–6135.

37 F. Yi, H. Ren, J. Shan, X. Sun, D. Wei and Z. Liu, Wearable energy sources based on 2D materials, *Chem. Soc. Rev.*, 2018, **47**(9), 3152–3188.

38 E. C. Ahn, 2D materials for spintronic devices, *npj 2D Mater. Appl.*, 2020, **4**(1), 17.

39 Y. Liu, C. Zeng, J. Zhong, J. Ding, Z. M. Wang and Z. Liu, Spintronics in two-dimensional materials, *Nano-Micro Lett.*, 2020, **12**(1), 93.

40 J. Hernández-Tecorralco, L. Meza-Montes, M. Cifuentes-Quintal and R. de Coss, Understanding the sp magnetism in substitutional doped graphene, *Phys. Rev. B*, 2022, **105**(22), 224425.

41 J.-Q. Wen, J.-M. Zhang, X. Yang and H. Wu, Computational research of electronic and magnetic properties of nonmetal doping of graphene-like ZnO monolayer, *J. Supercond. Novel Magn.*, 2018, **31**(6), 1833–1840.

42 A.-M. Hu, L.-l. Wang, W.-Z. Xiao, G. Xiao and Q.-Y. Rong, Electronic structures and magnetic properties in nonmetallic element substituted MoS_2 monolayer, *Comput. Mater. Sci.*, 2015, **107**, 72–78.

43 M. Luo, E. Xu Yu and X. Zhang Qiu, Magnetic properties of monolayer WSe_2 doped with nonmagnetic metal and nonmetal atoms, *AIP Adv.*, 2018, **8**(8), 085212.

44 M. Zhong, S. Zhang, L. Huang, J. You, Z. Wei, X. Liu and J. Li, Large-scale 2D PbI_2 monolayers: experimental realization and their indirect band-gap related properties, *Nanoscale*, 2017, **9**(11), 3736–3741.

45 D. Hoat, T. V. Vu, M. M. Obeid and H. R. Jappor, Assessing optoelectronic properties of PbI_2 monolayer under uniaxial strain from first principles calculations, *Superlattices Microstruct.*, 2019, **130**, 354–360.

46 Z.-H. Liu, C.-L. Yang, M.-S. Wang and X.-G. Ma, SiI_2 monolayer as a promising photocatalyst for water splitting hydrogen production under the irradiation of solar light, *Int. J. Hydrogen Energy*, 2020, **45**(35), 17517–17524.

47 C.-S. Liu, X.-L. Yang, J. Liu and X.-J. Ye, Exfoliated monolayer GeI_2: theoretical prediction of a wide-band gap semiconductor with tunable half-metallic ferromagnetism, *J. Phys. Chem. C*, 2018, **122**(38), 22137–22142.

48 D. Hoat, T. V. Vu, M. M. Obeid and H. R. Jappor, Tuning the electronic structure of 2D materials by strain and external electric field: case of GeI_2 monolayer, *Chem. Phys.*, 2019, **527**, 110499.

49 Q.-Q. Yuan, F. Zheng, Z.-Q. Shi, Q.-Y. Li, Y.-Y. Lv, Y. Chen, P. Zhang and S.-C. Li, Direct growth of van der Waals tin diiodide monolayers, *Adv. Sci.*, 2021, **8**(20), 2100009.

50 A. Betal, J. Bera and S. Sahu, Low-temperature thermoelectric behavior and impressive optoelectronic properties of two-dimensional XI_2 (X= Sn, Si): A first principle study, *Comput. Mater. Sci.*, 2021, **186**, 109977.

51 B. D. Aparicio-Huacarpuma, J. A. d. S. Laranjeira, K. A. Lopes Lima, E. A. Moujaes, A. M. A. Silva, J. Ricardo Sambrano, A. Cavalheiro Dias and L. A. Ribeiro Junior, Optoelectronic and excitonic study of XI_2 (X= Si, Ge, Sn, and Pb) monolayers envisaging potential technological applications, *ACS Omega*, 2025, **10**(48), 59219–59229.

52 Q.-Y. Xie, P.-F. Liu, J.-J. Ma, F.-G. Kuang, K.-W. Zhang and B.-T. Wang, Monolayer SnI_2: An excellent p-type thermoelectric material with ultralow lattice thermal conductivity, *Materials*, 2022, **15**(9), 3147.

53 Z. Shao, X. Wang, H. Qiu, H. Sun, Y. Cao, X. Wu and X. Chen, Phonon mode softening and band convergence induced significant enhancement of thermoelectric performance in strained CdI_2-type SnI_2 monolayer, *Results Phys.*, 2024, **58**, 107541.

54 W. Kohn and L. J. Sham, Self-consistent equations including exchange and correlation effects, *Phys. Rev.*, 1965, **140**(4A), A1133.

55 J. P. Perdew, K. Burke and M. Ernzerhof, Generalized gradient approximation made simple, *Phys. Rev. Lett.*, 1996, **77**(18), 3865.

56 A. V. Krukau, O. A. Vydrov, A. F. Izmaylov and G. E. Scuseria, Influence of the exchange screening parameter on the performance of screened hybrid functionals, *J. Chem. Phys.*, 2006, **125**(22), 224106.

57 S. Grimme, J. Antony, S. Ehrlich and H. Krieg, A consistent and accurate ab initio parametrization of density

functional dispersion correction (DFT-D) for the 94 elements H-Pu, *J. Chem. Phys.*, 2010, **132**(15), 154104.

58 G. Kresse and J. Furthmüller, Efficiency of ab-initio total energy calculations for metals and semiconductors using a plane-wave basis set, *Comput. Mater. Sci.*, 1996, **6**(1), 15–50.

59 G. Kresse and J. Furthmüller, Efficient iterative schemes for ab initio total-energy calculations using a plane-wave basis set, *Phys. Rev. B: Condens. Matter Mater. Phys.*, 1996, **54**(16), 11169.

60 H. J. Monkhorst and J. D. Pack, Special points for Brillouin-zone integrations, *Phys. Rev. B: Condens. Matter Mater. Phys.*, 1976, **13**(12), 5188.

61 A. Togo, L. Chaput, T. Tadano and I. Tanaka, Implementation strategies in phonopy and phono3py, *J. Phys. Condens. Matter*, 2023, **35**(35), 353001.

62 S. Nosé, A unified formulation of the constant temperature molecular dynamics methods, *J. Chem. Phys.*, 1984, **81**(1), 511–519.

63 W. G. Hoover, Canonical dynamics: Equilibrium phase-space distributions, *Phys. Rev.*, 1985, **31**(3), 1695.

64 F. Mouhat and F.-X. Coudert, Necessary and sufficient elastic stability conditions in various crystal systems, *Phys. Rev. B: Condens. Matter Mater. Phys.*, 2014, **90**(22), 224104.

65 S. Wang, J.-X. Li, Y.-L. Du and C. Cui, First-principles study on structural, electronic and elastic properties of graphene-like hexagonal Ti_2C monolayer, *Comput. Mater. Sci.*, 2014, **83**, 290–293.

66 M. Topsakal, S. Cahangirov and S. Ciraci, The response of mechanical and electronic properties of graphane to the elastic strain, *Appl. Phys. Lett.*, 2010, **96**(9), 091912.

67 K. Michel and B. Verberck, Theory of elastic and piezoelectric effects in two-dimensional hexagonal boron nitride, *Phys. Rev. B Condens. Matter*, 2009, **80**(22), 224301.

68 J. Deng, I. Fampiou, J. Liu, A. Ramasubramaniam and N. Medhekar, Edge stresses of non-stoichiometric edges in two-dimensional crystals, *Appl. Phys. Lett.*, 2012, **100**(25), 251906.

69 M. Naseri, D. Hoat, K. Salehi and S. Amirian, Theoretical prediction of 2D XI_2 (X= Si, Ge, Sn, Pb) monolayers by density functional theory, *J. Mol. Graph. Model.*, 2020, **95**, 107501.

70 M. Yagmurcukardes, F. M. Peeters and H. Sahin, Electronic and vibrational properties of PbI_2: From bulk to monolayer, *Phys. Rev. B*, 2018, **98**, 085431.